

Nonlinear quantum magnetophononics in $\text{SrCu}_2(\text{BO}_3)_2$

F. Giorgianni¹, B. Wehinger^{1,2,3}, S. Allenspach^{1,2}, N. Colonna^{1,4}, C. Vicario¹, P. Puphal^{1,5},
E. Pomjakushina¹, B. Normand^{1,6}, and Ch. Rüegg^{1,2,6,7}

¹Paul Scherrer Institute, CH-5232 Villigen-PSI, Switzerland.

²Department of Quantum Matter Physics, University of Geneva, CH-1211 Geneva 4, Switzerland.

³Department of Molecular Sciences and Nanosystems, Ca' Foscari University of Venice, 30172 Venezia Mestre, Italy.

⁴National Centre for Computational Design and Discovery of Novel Materials (MARVEL), Ecole Polytechnique Fédérale de Lausanne (EPFL), CH-1015 Lausanne, Switzerland

⁵Max Planck Institute for Solid State Research, Heisenbergstrasse 1, 70569 Stuttgart, Germany.

⁶Institute of Physics, Ecole Polytechnique Fédérale de Lausanne (EPFL), CH-1015 Lausanne, Switzerland.

⁷Institute of Quantum Electronics, ETH Zürich, CH-8093 Höggerberg, Switzerland.

*Correspondence to: flavio.giorgianni@psi.ch, christian.rueegg@psi.ch.

Harnessing the most advanced capabilities of quantum technologies will require the ability to control macroscopic quantum states of matter. Quantum magnetic materials provide a valuable platform for realizing highly entangled many-body quantum systems [1], and have been used to investigate phenomena ranging from quantum phase transitions (QPTs) [2-6] to fractionalization, topological order and the entanglement structure of the quantum wavefunction [7]. Although multiple studies have controlled their properties by static applied pressures [2-5] or magnetic fields [6], dynamical control at the fundamental timescales of their magnetic interactions remains completely unexplored. However, major progress in the technology of ultrafast laser pulses [8,9] has enabled the dynamical modification of electronic properties [10-13], and now we demonstrate the ultrafast control of quantum magnetism. This we achieve by a magnetophononic mechanism [14], the driving of coherent lattice displacements to produce a resonant excitation of the quantum spin dynamics. Specifically, we apply intense terahertz laser pulses to excite a collective spin state of the quantum antiferromagnet $\text{SrCu}_2(\text{BO}_3)_2$ [15-18] by resonance with the nonlinear mixing frequency of the driven phonons [19] that modulate the magnetic interactions. Our observations indicate a universal mechanism for controlling nonequilibrium quantum many-body physics on timescales many orders of magnitude faster than those achieved to date.

The dynamical control of quantum systems by using light to access their intrinsic interaction timescales opens new windows both on fundamental phenomena in nonequilibrium many-body physics and on applications in high-frequency data-processing. Coherent light sources developed to combine ultrafast time structure and high intensity at the appropriate terahertz

(THz) or mid-infrared frequencies [8,9] have been used in complex condensed matter to enhance superconductivity [10], drive metal-insulator transitions [11], manipulate multiferroic order [12] and “Floquet engineer” the electronic band structure [13]. Beyond the charge sector, however, probing the full richness of correlated quantum materials at the level of the many-body wavefunction requires extending such optical control to degrees of freedom including orbitals, nematicities, chiralities and especially spins.

Quantum magnets [1] offer some of the cleanest realizations in contemporary condensed-matter physics of simple model Hamiltonians that host complex quantum many-body states [7]. Among the different ways to control these states, we focus on the fact that experiments under pressure have created novel ground and excited states [2,3], switched the ground state by driving a QPT and controlled quantum criticality in both localized [4] and itinerant magnetic systems [5]. That such dramatic effects are obtained under static conditions demonstrates the extreme sensitivity of the magnetic interactions to the atomic positions, and hence the potential for dynamical control by the ultrafast driving of coherent lattice displacements.

In ultrafast studies of magnetism, the magnetic field of a light pulse can drive precessional spin dynamics and spin waves in ordered antiferromagnets by the Zeeman effect [20,21]. Strong lattice excitations have been used to induce spin waves through an effective magnetic field [22] and to melt magnetic order [23]. The concept of magnetophononics, i.e. exploiting the highly frequency-specific nature of the resonant spin-lattice interaction, has been discussed theoretically for ordered magnets [14]. Here we extend and apply it to control collective quantum spin states by using coherent THz pulses to drive infrared (IR)-active phonons in the quantum antiferromagnet $\text{SrCu}_2(\text{BO}_3)_2$ [15]. We demonstrate experimentally how coherent, light-induced atomic displacements control the nonequilibrium population of an excited spin state and establish the theoretical framework for the origin of this phenomenon, in the modulation of magnetic interactions caused by nonlinear phonon mixing, which we verify by density functional theory (DFT) calculations.

The two-dimensional Shastry-Sutherland model [24] is one of the most intriguing in quantum magnetism. Spins $S = 1/2$ with Heisenberg interactions on this perfectly frustrated orthogonal dimer network (Fig. 1a) have an exact dimer-singlet ground state when the ratio of interdimer (J') to intradimer (J) interactions satisfies $\alpha = J'/J \leq 0.675$, above which a QPT occurs to a plaquette-singlet state [25]. Quite remarkably, this model is realized in the compound $\text{SrCu}_2(\text{BO}_3)_2$ (Fig. 1b) [15], with J determined by Cu-O-Cu superexchange processes on the Cu^{2+} dimer units and J' by superexchange through the BO_3 units. The magnetic excitation spectrum of $\text{SrCu}_2(\text{BO}_3)_2$ contains the “triplon” (singlet-triplet) excitation at $\Delta = 2.9$ meV ($\Delta/h = 0.71$ THz), a strongly bound $S = 0$ two-triplon bound state (TBS) at $\hbar\omega_{\text{TBS}} = 3.6$ meV (0.87 THz), both depicted in Fig. 1a, and additional discrete and continuum $S = 1$ and $S = 2$ modes at higher energies. These modes have been studied by a combination of neutron scattering [16], Raman [17,18] and IR [26] spectroscopies, although a detailed explanation for the phonon-assisted coupling of light to the spin excitations observed in the Raman and IR experiments remains elusive due to their inherently incoherent nature. The interaction ratio in $\text{SrCu}_2(\text{BO}_3)_2$, $\alpha = 0.63$, lies close to the QPT of the Shastry-Sutherland model, and in fact this transition has been induced under a static pressure [3]. Very recently, attention has focused on

how the magnetic interactions depend on the geometry of the dimer units [27-29], making $\text{SrCu}_2(\text{BO}_3)_2$ a fascinating and timely candidate for exploring magnetophononic coupling on ultrafast timescales.

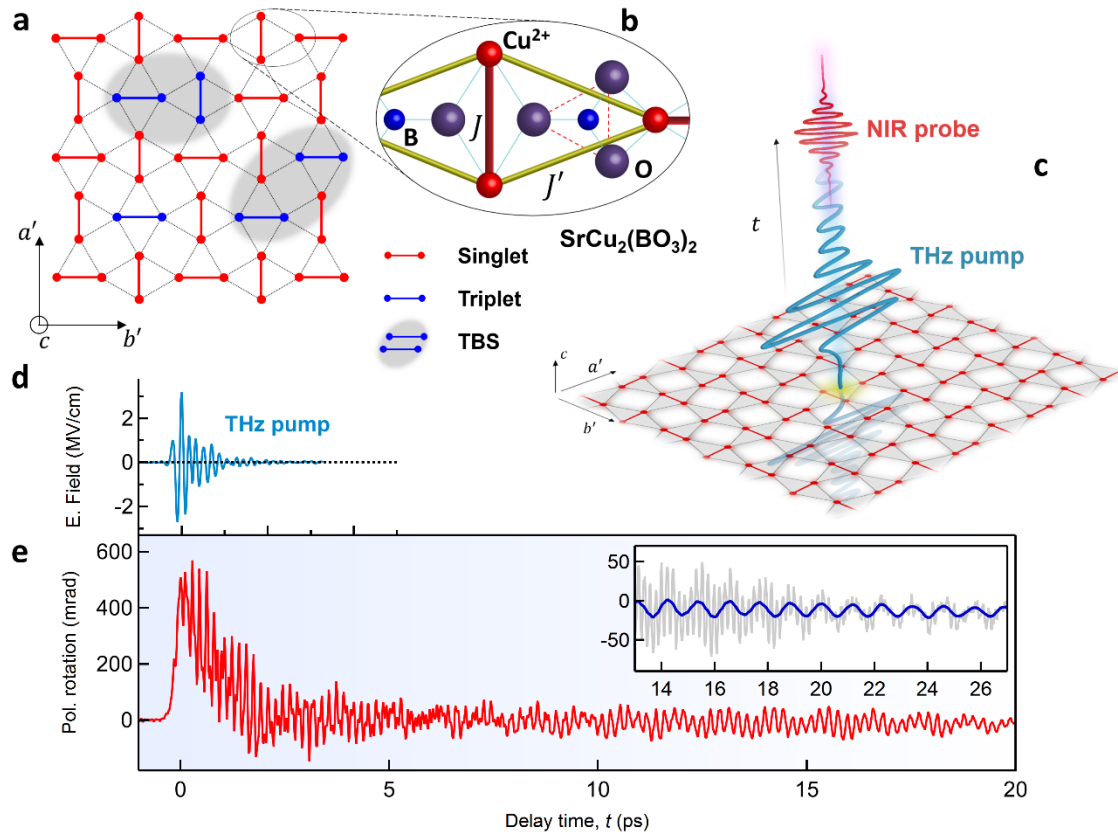


Fig. 1 | Atomic positions in $\text{SrCu}_2(\text{BO}_3)_2$ and a coherent lattice-control experiment in the time domain. **a**, Schematic representation of the spin network in $\text{SrCu}_2(\text{BO}_3)_2$ and of the low-energy spin excitations in the singlet ground state. Individual triplon excitations are shown as blue dimers and two-triplon bound states (TBS) as shaded grey areas. **b**, Lattice structure of $\text{SrCu}_2(\text{BO}_3)_2$ in the $a'b'$ -plane. Cu^{2+} ions ($S = 1/2$) form the two-dimensional Shastry-Sutherland network with interaction parameters J on the Cu-Cu dimers (red bonds) and J' between neighbouring orthogonal dimers (yellow bonds). **c**, Experimental set-up. An intense THz pulse (purple) with electric field linearly polarized along a' provides coherent driving of dipole-active lattice vibrations. A femtosecond near-IR (NIR) probe pulse (red) measures the polarization changes. **d-e**, THz electric field and polarization rotation of the probe as functions of the delay time, t . **Inset**: THz-driven dynamics after filtering of the fast component to reveal coherent oscillations at 0.87 THz associated with the TBS (blue).

Our experiments use a single-crystal sample (Methods) maintained at 3.5 K ($k_B T \ll \Delta$), a temperature where the ground state is close to the pure singlet state. We perform THz pump-probe optical spectroscopy with the apparatus [30] described in Sec. S1 of the Supplementary Information (SI) [31]. As represented in Fig. 1c, intense laser pulses (Fig. 1d) with spectral content between 2 and 7 THz are used to drive the resonant excitation of dipole-active phonon modes [32]. The ultrafast lattice and spin dynamics are probed by polarization rotation (Fig. 1e) [22], whose origin lies in optical birefringence and Faraday effects. These ultrafast

polarization changes are imprinted on the co-propagating NIR pulse (50 fs, wavelength 800 nm) and measured as a function of the delay time, t , as detailed in Sec. S2 of the SI [31].

As the inset of Fig. 1e makes clear, the 1 ps pulse creates dynamical oscillations that persist for tens of ps. We observe coherently excited phonons close to the peak of the pump spectrum (Fig. 2a), primarily two of the E -symmetric modes measured by IR spectroscopy [32], centred at $\omega_a = 3.78$ and $\omega_b = 4.60$ THz. Strikingly, we observe a strong response precisely at ω_{TBS} (Fig. 2b), even though the spectral content of the pump is negligible in this frequency range. The feature centred at 11.6 THz, much higher than the spectral content of the pump, is a Raman-active B_1 phonon mode, analysed in Sec. S3 of the SI [31], which indicates that nonlinear phonon coupling is allowing sum-frequency excitation processes.

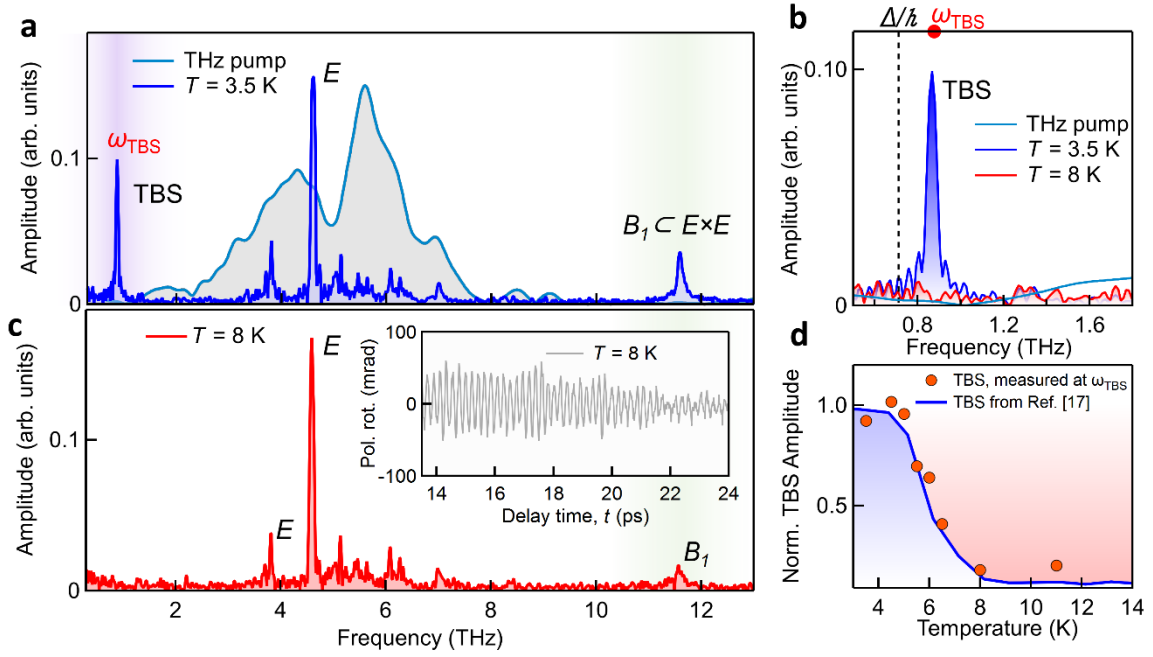


Fig. 2 | THz field-driven lattice and spin dynamics in the frequency domain. **a**, Spectral amplitude (blue) of the data of Fig. 1e computed for $3.5 \leq t \leq 20$ ps. The primary peaks are (i) E -symmetric phonons at 3.78 THz and 4.60 THz, (ii) a B_1 -symmetric Raman phonon at 11.6 THz and (iii) the TBS excitation at $\omega_{\text{TBS}} = 0.87$ THz. The purple curve shows the spectral amplitude of the driving electric field (Fig. 1d). **b**, Comparison of low-frequency spectra at 3.5 and 8 K. The black dashed line marks the one-triplon gap, $\Delta/h = 0.71$ THz, and the red dot ω_{TBS} from Raman spectroscopy [17,18]. **c**, Spectral amplitude measured at 8 K, where the TBS is absent and the driven dynamics reveal no coherent oscillations at ω_{TBS} (inset). **d**, Temperature-dependence of the TBS, normalized to the peak height.

To identify the excitation at 0.87 THz as the TBS, we repeated the experiment at 8 K (Figs. 2b-c), where thermal fluctuations cause the triplons to lose their character [33]. While the spectral features of the lattice remain almost unchanged, the magnetic fingerprint of THz driving has disappeared. As Fig. 2d makes clear, the measured amplitude shows rapid quenching above 5 K, exactly as observed for the TBS in Ref. [17], where this behaviour was attributed to strong scattering from thermally excited triplets. The reduced lifetime of the B_1 phonon in Fig. 2c also provides evidence of damping processes due to spin-lattice coupling.

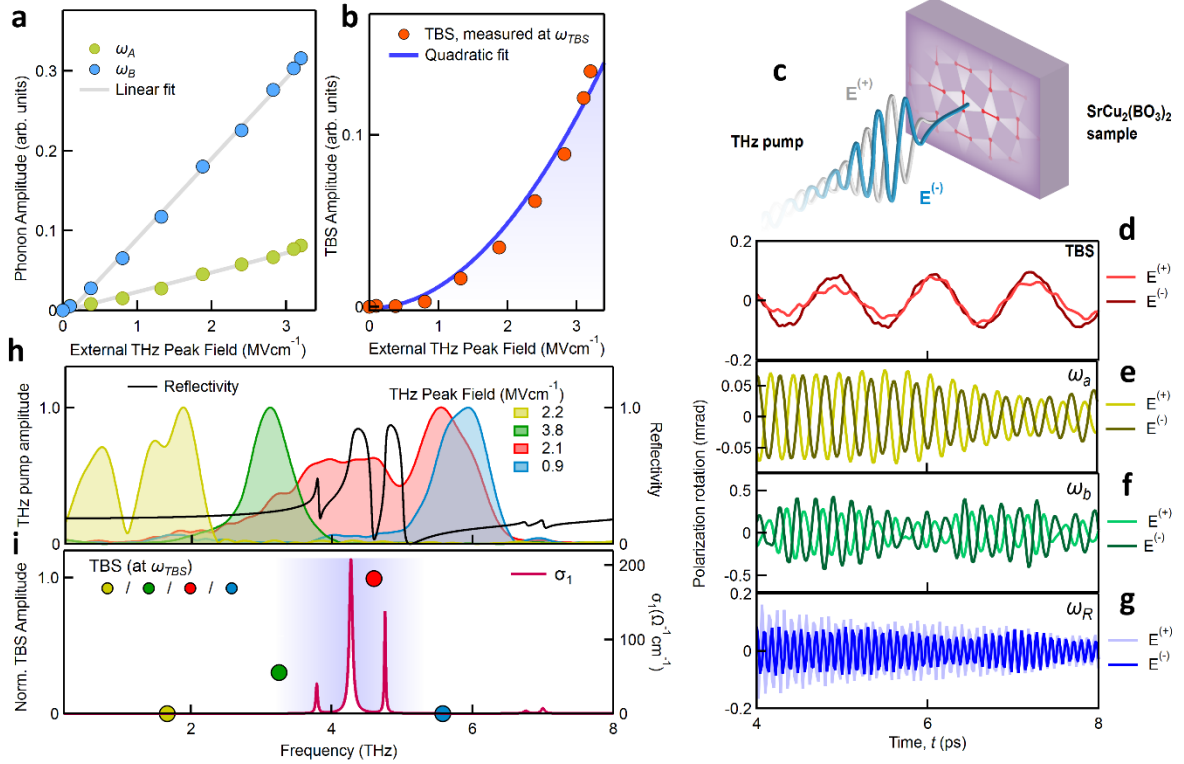


Fig. 3 | THz pump strength and frequency-dependence. **a**, Linear dependence of phonon amplitudes and **b**, quadratic dependence of the TBS amplitude on the electric-field strength. **c**, Representation of two THz pump pulses with inverted electric-field polarities, $E^{(+)}$ and $E^{(-)}$. **d-g**, Comparison of the dynamics of the magnetic and lattice modes for these two pump polarities. We note that perfect inversion of the IR phonon signals, and perfect overlap of the TBS and Raman phonon signals, are actually obtained for a time shift of -20 fs in the $E^{(-)}$ signal. This can be attributed to the fact that rotation of the THz generation crystal may generate a small time-delay in the event of an inhomogeneity in its thickness (20 fs corresponds to approximately $6 \mu\text{m}$ in vacuum). **h**, Four different normalized THz pump spectra shown together with the reflectivity of $\text{SrCu}_2(\text{BO}_3)_2$ at 4 K (calculated from Ref. [32]); peak field values for the corresponding spectra are indicated in the legend. **i**, TBS mode amplitude (coloured points), normalized to the square of the peak field, for different values of the THz pump-frequency centroid. Here we show for comparison the real part, $\sigma_1(\omega)$, of the optical conductivity.

To understand the mechanism driving a purely magnetic excitation, the fact that the spectral content of the pump contains negligible intensity below 2 THz excludes a direct coupling of light to the TBS, which in any case is not IR-active [26]. To probe the indirect origin of the observed spin dynamics, we measure the mode amplitudes as functions of the THz electric-field strength. The IR phonons display the linear dependence expected for resonant excitation (Fig. 3a). By contrast, the TBS amplitude varies quadratically with the field strength (Fig. 3b), and thus with lattice displacement, indicating a nonlinear coupling mechanism essentially different from electric or magnetic dipolar interactions [21,34]. Confirmation that this dependence is quadratic can be obtained by inverting the polarity of the driving electric field of the THz pump pulse, as represented in Fig. 3c. To implement this sign inversion experimentally, we rotate the crystal for THz generation by 180° and compare the driven

dynamics of the polarization-rotation signals. The results in the time domain, shown in Figs. 3d-g, confirm a phase shift of 180° for the E -symmetric phonon modes (Fig. 3e-f); because these are excited directly, the carrier-envelope phase of the THz pump is imprinted on the IR-active phonons. By contrast, the dynamics of the TBS (Fig. 3d) are invariant on changing the electric-field polarity, fully consistent with a quadratic driving mechanism. The dynamics of the Raman-active phonon at 11.6 THz, discussed in Sec. S3 of the SI, are similarly insensitive to the change of polarity, as shown in Fig. 3g. For a direct demonstration of which IR phonons provide the drive, we vary the spectral content of the pump (Fig. 3h) and measure the TBS amplitude, which again is large only when the pump spectrum covers ω_a and ω_b (Fig. 3i); there is no sign of coherent magnetic dynamics in off-resonant conditions, such as driving frequencies above 6 THz. This proves that the opto-magnetic coupling is mediated by the resonant lattice excitations and cannot be explained by nonlinear effects involving non-resonant electronic excitations, such as free-carrier generation by THz-induced electronic breakdown [35] or impact ionization [36].

We now establish the physical framework for the nonlinear quantum magnetophononic phenomenon we have created. Qualitatively, the lattice displacements due to any phonon excitation alter the instantaneous magnetic interactions (Fig. 4a). In a minimal model with two IR phonons, ω_a and ω_b , the net displacement is $q_t = q_a + q_b$. When the time-dependent perturbation of the spin Hamiltonian created by this phonon-induced modulation is expressed as a Taylor expansion [Eq. (3) of the Methods section], the q_t^2 terms lead to spectral components at beating frequencies $\omega_a + \omega_b$ and $\omega_b - \omega_a$, providing the nonlinear mechanism. The key to the unconventional physics of $\text{SrCu}_2(\text{BO}_3)_2$ at equilibrium is the exact frustration of the two interdimer coupling paths, J' , in Fig. 1b. This is broken in the driven, nonequilibrium lattice structure, and it is the finite values of $\Delta J' = J'_1 - J'_2$ (Fig. 4a) that allow a direct excitation of the TBS from the singlet quantum ground state ($|s\rangle$) [Methods Eq. (4)]. Because the driving phonons cannot change the magnetic state, they couple only to this $\Delta S_{tot} = 0$ process.

For a quantitative verification of this framework, we use Quantum Espresso [37] to perform density functional theory (DFT) calculations. First we compute the equilibrium lattice and magnetic structures, as summarized in the Methods section. We then perturb the lattice by the atomic displacements deduced from our experiments for the primary optically driven phonons [32], in order to estimate the phonon-induced modulation of the magnetic interaction parameters. Figure 4 summarizes the results described in Sec. S4 of the SI [31]. The DFT calculations become more involved for the symmetry-broken lattice (Fig. 4a), and in Fig. 4b we show the four different interdimer interaction parameters (J'_1, J'_2, J'_3, J'_4) neighbouring each spin dimer as functions of the scalar phonon displacement amplitude, q_b , whose maximum value is approximately 0.17 \AA [Methods Eq. (2)]. While the variations in J are almost quadratic, the interactions $J'_{1..4}$ all have significant linear components, which result in finite differences, $\Delta J'$, of order 10 K (Fig. 4b). Extending these results into the time domain, in Fig. 4c we show q_t and in Fig. 4d the resulting evolution of $\Delta J' = J'_1 - J'_2$. In the frequency domain, the IR phonons excited by the THz pump (Fig. 4e) create a nonlinear modulation of the interaction parameters with a rich spectrum (Fig. 4f). This spectrum includes significant weight at the frequency $\omega_b - \omega_a$, whose resonance with the TBS (inset, Fig. 4e) ensures large values of the

matrix element for two-triplon creation, $\langle \text{TBS} | \Delta J'(\omega) t_{1i}^\dagger t_{2j}^\dagger | S \rangle$, and hence the strong nonequilibrium population of this purely magnetic excitation that we report in Figs. 2a and 2b, completing the explanation of magnetophononic driving.

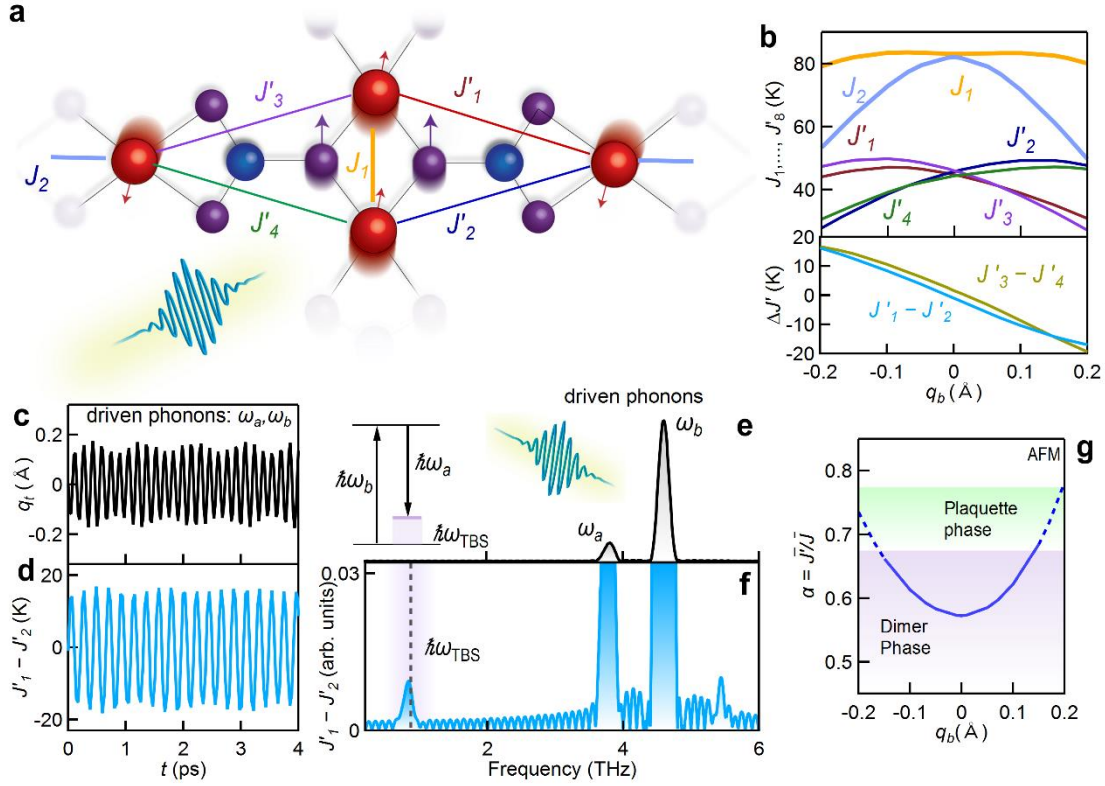


Fig. 4 | Dynamic control of magnetic interactions by light-driven phonons. **a**, Schematic representation of atomic motions in the ab -plane associated with the $\omega_b = 4.60$ THz phonon. **b**, Interaction parameters $J, J'_1, J'_2, J'_3, J'_4, \Delta J_{12}$ and ΔJ_{34} calculated for the symmetry-broken lattice structure as functions of the corresponding phonon displacement, q_b . **c**, Temporal modulation of $q_a + q_b$ calculated using the experimental THz driving field. **d**, Corresponding dynamic modulation of $\Delta J'_{12}$. **e**, Spectrum of driven IR phonons, with weight only at the frequencies ω_a and ω_b . Inset: energy-level diagram of the TBS excitation process, which is a resonance between the phonon frequency difference, $\omega_b - \omega_a$, and ω_{TBS} . **f**, Fourier transform of the DFT time series for $\Delta J'_{12}(t)$, showing spectral weight at ω_{TBS} . **g**, Interaction ratio, $\alpha = \bar{J}'/\bar{J}$, where $\bar{J} = \frac{1}{2}(J_1 + J_2)$ and $\bar{J}' = \frac{1}{8}(\bar{J}'_1 + \dots + \bar{J}'_8)$, shown as a function of q_b .

Figure 4g indicates that our method of driving multiple IR-active phonons in the harmonic regime causes a strong increase in the instantaneous ratio of the spatially averaged interactions, $\alpha = \bar{J}'/\bar{J}$, and hence offers a route towards the QPT into the plaquette phase of $\text{SrCu}_2(\text{BO}_3)_2$. While recent experimental [27] and theoretical [28] studies have highlighted the role of the ‘‘pantograph’’ phonon [29] in modulating α , this A_1 -symmetric mode, found at 6.1 THz in Raman measurements, cannot be excited coherently in the same way as IR phonons. In either case, the phonons are very fast processes on the timescale of the magnetic interactions, and hence the important quantity is the time-average of $\alpha(q_t)$ in Fig. 4g. We remark that this is also why the IR phonons we drive do not cause a detectable alteration of the excitation energy, ω_{TBS} , only of the mode population. Our studies indicate the potential for large increases in THz field strength and for detailed tailoring of the excited phonon modes to achieve significantly

stronger effects than those represented in Fig. 4g. Such a light-driven crossing of the average α through the QPT would then be dynamic in origin but static on the natural timescale of the spin dynamics.

One may question whether further terms in the modulated spin Hamiltonian could allow the observation of spin excitations that are normally weak or forbidden. SrCu₂(BO₃)₂ has Dzyaloshinskii-Moriya (DM) interactions [38], which are small (3% of J), but are important in applied magnetic fields, including to create topological states [16]. The driving of symmetry-breaking IR phonons also creates dynamical antisymmetric spin interactions directly analogous to the modulation of J and J' . In SrCu₂(BO₃)₂, our experiments demonstrate no discernible role for driven DM interactions, because the one-triplon excitation process ($\Delta S_{tot} = 1$) at 0.71 THz should be excited by the same difference-frequency envelope as the TBS, but clearly no feature is visible above the detection threshold at this frequency in Fig. 2b. More generally, however, one may use IR phonon driving to manipulate both the symmetric and antisymmetric magnetic interactions in systems such as chiral spin liquids and skyrmion lattices, where both play an essential role.

In summary, we have demonstrated a general approach to induce coherent light-driven spin dynamics by a lattice-mediated resonant mechanism. At the most fundamental level, our results provide a qualitatively new and attractive route for the dynamic control of correlated quantum systems, opening an additional time dimension for exploring phenomena probed to date only by quasi-static stimuli. Our methods can excite states forbidden at equilibrium and create coherent nonequilibrium spin populations that lead to novel transient phenomena, such as light-induced Bose-Einstein condensation or topological magnetic phases. By the resonant excitation of phonons and their nonlinear mixing to span a very wide (sum and difference) frequency range, our experimental protocol meets the intrinsic challenge of spin-phonon frequency-matching and hence is applicable to all the exotic spin states available in quantum magnetic materials. In view of ongoing technical progress at all the frontiers of narrow-band spectra, high intensities and ultrashort pulses, there is wide scope for order-of-magnitude improvements in both driving and detection. The result will be a toolbox for quantum control of collective states in tailored nonequilibrium conditions that promises profound new insight into time-dependent quantum many-body physics.

- [1] Sachdev, S. Quantum magnetism and criticality. *Nat. Phys.* **4**, 173–185 (2008).
- [2] Rüegg, Ch. *et al.* Quantum Magnets under Pressure: Controlling Elementary Excitations in TiCuCl₃. *Phys. Rev. Lett.* **100**, 205701 (2008).
- [3] Zayed, M. E. *et al.* 4-spin plaquette singlet state in the Shastry-Sutherland compound SrCu₂(BO₃)₂. *Nat. Phys.* **13**, 962–966 (2017).
- [4] Merchant, P. *et al.* Quantum and classical criticality in a dimerized quantum antiferromagnet. *Nat. Phys.* **10**, 373–379 (2014).
- [5] Uhlarz, M., Pfleiderer, C. & Hayden, S. M. Quantum Phase Transitions in the Itinerant Ferromagnet ZrZn₂. *Phys. Rev. Lett.* **93**, 256404 (2004).
- [6] Giamarchi, T., Rüegg, Ch. & Tchernyshyov, O. Bose-Einstein condensation in magnetic insulators. *Nat. Phys.* **4**, 198–204 (2008).

- [7] Broholm, C. *et al.* Quantum spin liquids. *Science* **367**, eaay0668 (2020).
- [8] Salén, P. *et al.* Matter manipulation with extreme terahertz light: Progress in the enabling THz technology. *Phys. Rep.* **836–837**, 1–74 (2019).
- [9] Nicoletti, D. & Cavalleri, A. Nonlinear light–matter interaction at terahertz frequencies. *Adv. Opt. Photonics* **8**, 401 (2016).
- [10] Mitrano, M. *et al.* Possible light-induced superconductivity in K_3C_{60} at high temperature. *Nature* **530**, 461–464 (2016).
- [11] Caviglia, A. D. *et al.* Ultrafast Strain Engineering in Complex Oxide Heterostructures. *Phys. Rev. Lett.* **108**, 136801 (2012).
- [12] Kubacka, T. *et al.* Large-Amplitude Spin Dynamics Driven by a THz Pulse in Resonance with an Electromagnon. *Science* **343**, 1333–1336 (2014).
- [13] Oka, T. & Kitamura, S. Floquet Engineering of Quantum Materials. *Annu. Rev. Condens. Matter Phys.* **10**, 387–408 (2019).
- [14] Fechner, M. *et al.* Magnetophononics: Ultrafast spin control through the lattice. *Phys. Rev. Mater.* **2**, 064401 (2018).
- [15] Miyahara, S. & Ueda, K. Theory of the orthogonal dimer Heisenberg spin model for $SrCu_2(BO_3)_2$. *J. Phys: Condens. Matter* **15**, R327–R366 (2003).
- [16] McClarty, P. A. *et al.* Topological triplon modes and bound states in a Shastry-Sutherland magnet. *Nat. Phys.* **13**, 736–741 (2017).
- [17] Lemmens, P. *et al.* Collective Singlet Excitations and Evolution of Raman Spectral Weights in the 2D Spin Dimer Compound $SrCu_2(BO_3)_2$. *Phys. Rev. Lett.* **85**, 2605–2608 (2000).
- [18] Gozar, A., Dennis, B. S., Kageyama, H. & Blumberg, G. Symmetry and light coupling to phononic and collective magnetic excitations in $SrCu_2(BO_3)_2$. *Phys. Rev. B* **72**, 064405 (2005).
- [19] Melnikov, A. A. *et al.* Coherent phonons in a Bi_2Se_3 film generated by an intense single-cycle THz pulse. *Phys. Rev. B* **97**, 214304 (2018).
- [20] Vicario, C. *et al.* Off-resonant magnetization dynamics phase-locked to an intense phase-stable terahertz transient. *Nat. Photonics* **7**, 720–723 (2013).
- [21] Kampfrath, T. *et al.* Coherent terahertz control of antiferromagnetic spin waves. *Nat. Photonics* **5**, 31–34 (2011).
- [22] Nova, T. F. *et al.* An effective magnetic field from optically driven phonons. *Nat. Phys.* **13**, 132–136 (2017).
- [23] Först, M. *et al.* Spatially resolved ultrafast magnetic dynamics initiated at a complex oxide heterointerface. *Nat. Mater.* **14**, 883–888 (2015).
- [24] Shastry, B. S. & Sutherland, B. Exact ground state of a quantum mechanical antiferromagnet. *Physica B+C*. **108**, 1069–1070 (1981).
- [25] Corboz, P. & Mila, F. Tensor network study of the Shastry-Sutherland model in zero magnetic field. *Phys. Rev. B* **87**, 115144 (2013).
- [26] Rööm, T. *et al.* Far-infrared study of the two-dimensional dimer spin system $SrCu_2(BO_3)_2$. *Phys. Rev. B*. **61**, 14342–14345 (2000).
- [27] Radtke, G., Saúl, A., Dabkowska, H. A., Salamon, M. B. & Jaime, M. Magnetic nanopantograph in the $SrCu_2(BO_3)_2$ Shastry-Sutherland lattice. *Proc. Natl. Acad. Sci. U. S. A.* **112**, 1971–1976 (2015).

- [28] Bettler, S., Stoppel, L., Yan, Z., Gvasaliya, S. & Zheludev, A. Sign switching of dimer correlations in SrCu₂(BO₃)₂ under hydrostatic pressure. *Phys. Rev. Res.* **2**, 012010 (2020).
- [29] Badrtdinov, D. I., Tsirlin, A. A., Mazurenko, V. V. & Mila, F. SrCu₂(BO₃)₂ under pressure: A first-principles study. *Phys. Rev. B* **101**, 224424 (2020).
- [30] Vicario, C., Trisorio, A., Allenspach, S., Rüegg, Ch. & Giorgianni, F. Narrow-band and tunable intense terahertz pulses for mode-selective coherent phonon excitation. *Appl. Phys. Lett.* **117**, 101101 (2020).
- [31] Supplementary Information is available at <http://xxx.yyy.zzz>.
- [32] Homes, C. C. *et al.* Infrared spectra of the low-dimensional quantum magnet SrCu₂(BO₃)₂: Measurements and *ab initio* calculations. *Phys. Rev. B* **79**, 125101 (2009).
- [33] Zayed, M. E. *et al.* Correlated Decay of Triplet Excitations in the Shastry-Sutherland Compound SrCu₂(BO₃)₂. *Phys. Rev. Lett.* **113**, 067201 (2014).
- [34] Schlauderer, S. *et al.* Temporal and spectral fingerprints of ultrafast all-coherent spin switching. *Nature* **569**, 383–387 (2019).
- [35] Yamakawa, H. *et al.* Mott transition by an impulsive dielectric breakdown. *Nat. Mater.* **16**, 1100–1105 (2017).
- [36] Tarekegne, A. T., Hirori, H., Tanaka, K., Iwaszczuk, K. & Jepsen, P. U. Impact ionization dynamics in silicon by MV/cm THz fields. *New J. Phys.* **19**, 123018 (2017).
- [37] Giannozzi, P. *et al.* Advanced capabilities for materials modelling with Quantum ESPRESSO. *J. Phys. Condens. Matter* **29**, 465901 (2017).
- [38] Nojiri, H., Kageyama, H., Ueda, Y. & Motokawa, M. ESR Study on the Excited State Energy Spectrum of SrCu₂(BO₃)₂ –A Central Role of Multiple-Triplet Bound States– *J. Phys. Soc. Jpn.* **72**, 3243–3253 (2003).

Methods

Crystal

Single crystals of SrCu₂(BO₃)₂ were grown using an optical floating-zone furnace (FZ-T-10000-H-IV-VP-PC, Crystal System Corp., Japan) with four 300 W halogen lamps as the heat source. The growth rate was 0.25 mm/h, with both feeding and seeding rods being rotated at approximately 15 rpm in opposite directions to ensure the homogeneity of the liquid; an argon atmosphere with 20% oxygen was maintained at 5 bar during growth. The high structural quality and orientation of the resulting single crystal was confirmed by x-ray diffraction and the high magnetic quality (absence of impurities) by susceptibility measurements. The crystal was cut using a diamond wire saw and cleaved along the *a'b'*-plane to give a sample of dimensions 1×3×0.24 mm³ that was used for the experiments.

Calculation of atomic displacement driven by the terahertz electric field

The external THz electric-field strength of the pump pulses shown in Fig. 1d was estimated from the formula [39]

$$E_{THz} = \sqrt{\frac{z_0 E_p 4\sqrt{\ln 2}}{\pi\sqrt{\pi} W^2 \tau_{FWHM}}}, \quad (1)$$

where z_0 is the vacuum impedance, $E_p = 0.8 \mu\text{J}$ is the THz pulse energy, $w = 92 \mu\text{m}$ is the beam waist and $\tau_{FWHM} = 0.21 \text{ ps}$ is the pulse duration taken from the full width at half-maximum height (FWHM). Thus we obtain $E_{THz} = 3.2 \text{ MVcm}^{-1}$. The peak polarization, P_m , induced by the THz pulse resonant with a generic phonon mode m is [10]

$$P_m = \frac{\sigma_1(\omega_m)}{\omega_m} \tilde{E}_{THz}, \quad (2)$$

where ω_m is the angular frequency and $\sigma_1(\omega_m)$ the optical conductivity of the driven phonon. The polarization arises from the modulation of the dipole moment of the crystal, $P_m = n_d \delta_m \mu_m$, where $\mu_m = e |\sum_{im} \hat{u}_{im} Z_{eff}^i|$ is the magnitude of the charge displacement due to phonon mode m , \hat{u}_{im} is the normalized vector of displacements of each atom i in phonon mode m , Z_{eff}^i are the Born effective charges of each atom, n_d is the number of dipoles per unit volume and δ_m is the maximum displacement coordinate of the phonon. The driving field, $\tilde{E}_{THz} = \beta_m E_{THz}$ in Eq. (2), is the effective electric field inside the sample acting on the phonon [40], where $\beta_m = 1 - R_m$ is determined by the reflectivity at frequency ω_m .

To estimate the value of δ_b induced by the THz field for phonon mode b at 4.60 THz (Fig. 4), we use $\omega_b = 2\pi \cdot 4.6 \times 10^{12} \text{ s}^{-1}$, $\sigma_1(\omega_b) = 137 \Omega^{-1}\text{cm}^{-1}$ from Ref. [32], $n_d = V^{-1}$ with $V = 5.71 \times 10^{-22} \text{ cm}^{-3}$ the volume of the unit cell and the value $\mu_b = 0.6e$ taken from our DFT calculations, as discussed in Sec. S4 of the SI [31]. The bandwidth of the external THz field, approximately 2.7 THz FWHM (Fig. 2a), is large compared to the linewidth of the phonon mode (0.1 THz FWHM, Fig. 3h), and by accounting for the reflection of the external field (Fig. 3h) we estimate $\beta_b \approx 0.02$. Thus we deduce a maximum displacement of $\delta_b = 0.17 \text{ \AA}$, which is comparable to that estimated in SrTiO_3 [40]. We stress that δ_m represents the maximum displacement of the most displaced O ion in the $\text{SrCu}_2(\text{BO}_3)_2$ structure due to phonon mode m , and that the corresponding displacements of all the Cu ions are far smaller, whence there is no danger of approaching the Lindemann melting criterion. Because the temporal duration of the pump pulse is approximately 0.5 ps (Fig. 1d), there is also no danger that the THz driving will increase the sample temperature.

Calculation of magnetic interaction parameters

The magnetic interaction parameters were calculated self-consistently by mapping the magnetic contribution to the total energies obtained from density functional theory (DFT) for different collinear spin configurations onto a Heisenberg Hamiltonian,

$$H = H_0 + H_H = H_0 + J \sum_{\langle ij \rangle} \vec{S}_i \cdot \vec{S}_j + J' \sum_{\langle\langle ij \rangle\rangle} \vec{S}_i \cdot \vec{S}_j, \quad (3)$$

where H_0 is spin-independent and H_H is the Shastry-Sutherland model: \vec{S}_i is spin-1/2 operator located on the Cu^{2+} ion at site i , J and J' are the magnetic interactions depicted in Fig. 1b and $\langle ij \rangle$ and $\langle\langle ij \rangle\rangle$ denote respectively pairs of sites on intra- and interdimer bonds. The magnetic interaction parameters were calculated using the Quantum Espresso package [37], an open-source tool for electronic structure calculations based on DFT and the pseudopotential plane-wave technique. Exchange and correlation effects were modelled using the PBE functional [41], augmented by a Hubbard U term to include the strongly correlated nature of the Cu 3d electrons. The calculation of magnetic interactions is a self-consistent process in which the

lattice structure is fully relaxed in the antiferromagnetic spin configuration for each fixed value of the effective U parameter and the energies of four different magnetic configurations are compared [42] to determine equilibrium values for J and J' . The full details of this process and of its intrinsic accuracy are presented in Sec. S4 of the SI. In the first step of our calculations we used this procedure to refine U , deducing that $U = 11.4$ eV yields the magnetic interactions $J = 7.24$ meV (84.0 K) and $J' = 4.28$ meV (49.7 K), in good agreement with experimental findings [16] and yielding a coupling ratio $\alpha = 0.592$ for the equilibrium lattice structure. We then extended these methods to evaluate the magnetic interactions in a large number of different “frozen phonon” configurations of the lattice. In these calculations, each atom in the structure of $\text{SrCu}_2(\text{BO}_3)_2$ was displaced by $q_m \hat{u}_{im}$, where q_m is the instantaneous displacement amplitude of excited phonon mode m and \hat{u}_{im} denotes the set of normal-mode vectors taken from Ref. [32]. These atomic displacements reduce the lattice symmetry and hence require more complex calculations of the interaction parameters in a larger unit cell, as detailed in Sec. S4 of the SI.

Phonon-driven two-triplon bound-state dynamics

The Hamiltonian of the pumped system is $H = H_0 + H_H + H_D + V_{ph} + H_{Em-ph}$, where V_{ph} is the phonon potential and $H_{Em-ph} = \sum_m \mu_m q_m E_{\text{THz}}$, the dipole coupling between the lattice and the THz light, is the term driving the excitation of IR-active (E -symmetric) phonon modes. The coherent lattice deformation due to all of these phonon modes, $q_t = \sum_m q_m$, creates a nonlinear modulation of the magnetic interaction parameters, causing additional coupled spin-phonon terms to enter the Hamiltonian, which we collect in H_D . To separate the phonon modulation terms in H_D , it is convenient to perform a Taylor expansion of the magnetic interactions, J and J' , in powers of the simultaneously driven coherent IR phonon coordinates, which we denote as q_m, q_n, \dots . Denoting an arbitrary interaction term as \tilde{J} , we obtain

$$\tilde{J}(q_m, q_n, \dots) = \tilde{J}(0) + \left. \frac{\partial \tilde{J}}{\partial q_m} \right|_{q=0} q_m + \left. \frac{\partial^2 \tilde{J}}{\partial q_m \partial q_n} \right|_{q_m, q_n=0} q_m q_n + \dots, \quad (4)$$

where the first term is part of H_H and the higher terms make clear the direct dependence of the additional contributions on the oscillating phonon coordinates.

Turning to the spin part of H_H and H_D , the key property of the Shastry-Sutherland model giving rise to its many exotic properties is the exact frustration of spin correlations between dimers. Thus the term $\vec{S}_i \cdot \vec{S}_j$ acting on a single dimer is an eigenoperator and when acting between dimers it is exactly cancelled by a second $\vec{S}_i \cdot \vec{S}_j$ term with equal size (J') and effectively opposite sign (Fig. 1b). The key qualitative effect of the excited phonons driving the lattice out of equilibrium is to allow a finite interdimer coupling, $\Delta J_{12} = J_1'(q_m, q_n, \dots) - J_2'(q_m, q_n, \dots)$, for the lowest-order matrix element connecting nearest-neighbour dimers. The processes creating the TBS are made most transparent by reexpressing the nonequilibrium spin Hamiltonian in the language of triplet creation and annihilation operators [16], which represent the excitation of the dimer (J) units in Fig. 1b into their triplet states. Treating the singlets as a scalar term gives rise, with reference to the notation of Fig. S4 of the SI, to the form

$$H_D = \sum_i [\Delta J_{12} (t_{1i}^\dagger t_{2i+x} + t_{1i}^\dagger t_{2i+x}^\dagger) + \Delta J_{34} (t_{2i}^\dagger t_{1i+x} + t_{2i}^\dagger t_{1i+x}^\dagger) + \Delta J_{56} (t_{1i}^\dagger t_{2i+y} + t_{1i}^\dagger t_{2i+y}^\dagger) + \Delta J_{78} (t_{2i}^\dagger t_{1i+y} + t_{2i}^\dagger t_{1i+y}^\dagger)] + H.c., \quad (5)$$

in which the first term in each bracket describes the propagation of existing triplon excitations and the second describes triplon pair creation. While the triplons are initially created on adjacent dimers, on the timescale of the spin system they will optimize their relative configuration within the $S = 0$ component of the TBS [16], as depicted in Fig. 1a. Because lattice excitations cannot change spin quantum numbers at the level of the present analysis, only transitions to the $S = 0$ component of the TBS are allowed. The prefactors in Eq. (5), ΔJ_{12} , ... ΔJ_{78} , make clear that this process is a phonon-driven triplon pair creation.

For a fully quantitative calculation of the nonlinear effects of the driven phonons, we follow Ref. [19] by considering $H_D(q_m, q_n)$ as a dynamic perturbation through the coupling term H_{Em-ph} . In the experiment we drive two different IR-active coherent phonon modes, a and b , simultaneously. The equations of motion of the lattice are

$$\begin{cases} \ddot{q}_a + \gamma_a \dot{q}_a + \omega_a^2 q_a = -B_a E_{THz}(t), \\ \ddot{q}_b + \gamma_b \dot{q}_b + \omega_b^2 q_b = -B_b E_{THz}(t), \end{cases} \quad (6)$$

where $\omega_a = 3.78$ THz and $\omega_b = 4.60$ THz are the experimental phonon frequencies, $\gamma_a = 0.02$ THz and $\gamma_b = 0.03$ THz are their respective damping rates [32] and E_{THz} is the external THz driving field taken from experiment (Fig. 1d). B_a and B_b are the dipolar coupling constants, which depend on the effective charges (Z_{eff}^i), the transmission coefficients (β_m) and the reduced masses of the phonon modes; here we deduce them from the maximum displacements of $\delta_a = 0.04$ Å and $\delta_b = 0.17$ Å calculated using Eq. (2). From Eq. (6) we compute the net atomic displacement due to the two leading phonon modes, $q_t = q_a + q_b$, as a function of time, obtaining the result shown in Fig. 4c. We then use our DFT calculations to obtain the temporal evolution of the difference in interdimer interaction parameters, $\Delta J'(t)$, reported in Fig. 4d.

- [39] Thomson, M. D., Kreß, M., Löffler, T. & Roskos, H. G. Broadband THz emission from gas plasmas induced by femtosecond optical pulses: From fundamentals to applications. *Laser Photonics Rev.* **1**, 349–368 (2007).
- [40] Kozina, M. *et al.* Terahertz-driven phonon upconversion in SrTiO₃, *Nat. Phys.* **15**, 387–392 (2019).
- [41] Perdew, J. P., Burke, K. & Ernzerhof, M. Generalized Gradient Approximation Made Simple. *Phys. Rev. Lett.* **77**, 3865–3868 (1996).
- [42] Radtke, G., Saúl, A., Dabkowska, H. A., Gaulin, B. D. & Botton, G. A. Electronic structure of the quasi-two-dimensional spin-gap system SrCu₂(BO₃)₂: Experiment and theory. *Phys. Rev. B* **77**, 125130 (2008).

Data Availability

The data that support the findings of this study are available from the corresponding author upon reasonable request.

Code Availability

The code used to perform all DFT calculations that support the findings of this study is available at www.quantum-espresso.org.

Acknowledgments We are grateful to C. Homes for sharing the calculated phonon eigenvectors. We thank T. Cea, M. Först, S. Furuya, R. Mankowsky, A. Razpopov and R. Valentí for valuable discussions. This research was supported by the European Research Council (ERC) within the EU Horizon 2020 research and innovation programme under Grant No. 681654 (HyperQC) and by the MARVEL National Centre of Competence in Research of the Swiss National Science Foundation.

Author contributions F.G., B.W. and Ch.R. designed the study. E.P. grew the single crystals. E.P. and P.P. characterized the crystals. B.W. and P.P. prepared the samples. F.G., B.W., S.A. and C.V. performed the experiments and analysed the data. B.N. provided the theoretical framework with contributions from F.G., B.W., S.A., N.C. and Ch.R. F.G. and N.C. performed DFT calculations with input from B.N. F.G., B.N. and Ch.R. wrote the manuscript with input from all the authors.

Competing Interests The authors declare no competing interests.

Additional Information

Correspondence and requests for materials should be addressed to F.G.

Supplementary Information for

Nonlinear quantum magnetophononics in $\text{SrCu}_2(\text{BO}_3)_2$

F. Giorgianni, B. Wehinger, S. Allenspach, N. Colonna, C. Vicario, P. Puphal,
E. Pomjakushina, B. Normand, and Ch. Rüegg

Section S1. Experimental set-up

The THz pump and optical probe set-up is shown in Fig. S1 [S1]. The output of a 20 mJ, 55 fs, 800nm Ti:sapphire laser was used to drive an optical parametric amplifier (OPA), which provides multi-mJ, ultrashort pulses [S2]. Single-cycle THz pulses were generated by optical rectification, using a crystal of DAST (4-N,Ndimethylamino-4'-N'-methyl-stilbazolium tosylate, from Rainbow Photonics), of the OPA signal at $1.5 \mu\text{m}$. Three low-pass filters, two with a 20 THz cut-off frequency and one with 10 THz, were used after the THz generation step to block the residual OPA beam, and gave an extinction ratio for the pump in excess of 10^5 . For the pump pulses, an additional high-pass filter with a cut-off of 4.2 THz was used to drive the primary IR-active phonons while ensuring a negligible spectral weight at the frequency of the leading magnetic modes (Fig. 2a of the main text). To select the four different pump pulses shown in Fig. 3h of the main text, we used respectively a 2 THz low-pass filter, a 3 THz band-pass filter, a 4.2 THz high-pass filter coupled with a 6 THz low-pass filter and a 6 THz band-pass filter. Our peak electric fields were reached by tight focusing of the THz beam using three parabolic mirrors [S2]. For the measurement of properties dependent on the pump strength, the THz electric field was tuned by three wire-grid polarizers.

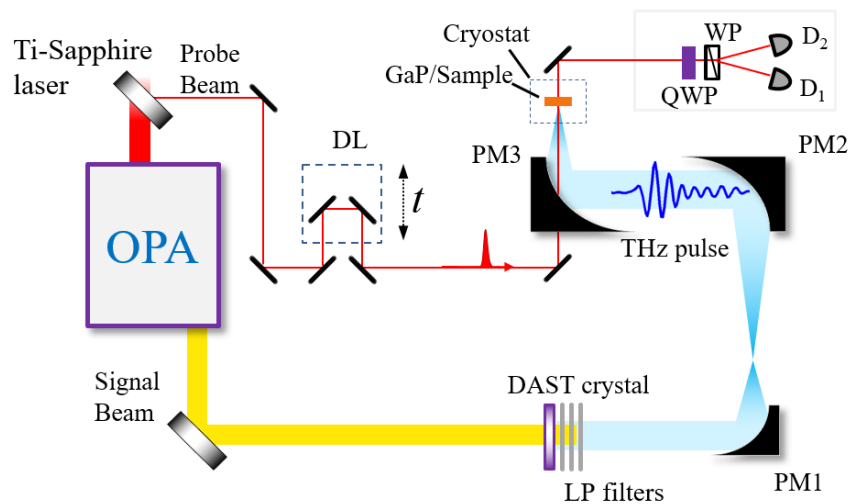


Fig. S1 | Experimental schematic of the THz-pump optical-probe set-up. Shown are the Optical Parametric Amplifier (OPA), parabolic mirrors (PM1-PM3), delay line (DL), quarter-wave plate (QWP), Wollaston prism (WP) and detectors (D1-D2).

The pump THz electric field in the sample plane was polarized along the direction perpendicular to the optical table. The temporal waveforms of the pump were measured at the sample position by electro-optic sampling in a $200 \mu\text{m}$ -thick (110) GaP crystal with a 50 fs,

800 nm gating pulse obtained as a fraction of the Ti:sapphire beam. The gating pulse was used to probe the ultrafast pump-induced polarization dynamics of the sample. The polarization of the probe relative to the sample was offset by 45° from the pump polarization. The THz-induced polarization changes caused by passage through the sample were measured by splitting the probe beam into two orthogonal components with a Wollaston prism. All measurements were performed in a He cryostat, which allowed a minimum background sample temperature of 3.5 K to be reached.

Section S2. Time-frequency analysis of THz-driven dynamics and mode symmetries

Figure S2 reports the temporal profile and frequency content measured for the THz pump pulse (Fig. S2a) and the resulting polarization rotations induced in the $\text{SrCu}_2(\text{BO}_3)_2$ sample at 4 K (Fig. S2b). The spectral decomposition was computed using a Hamming sliding-window fast Fourier transform. It is clear that the distribution of frequencies in the THz pump pulse (Fig. S2a) causes not only a direct resonant driving of E -symmetric, IR-active phonons but also a less direct, nonlinear driving of B_1 -symmetric, Raman-active phonons at higher frequencies (Figs. S2b and S2c); for this the low-temperature point group, D_{2d} (space group $I\bar{4}2m$), permits the excitation of $B_1 (\subset E \times E)$ phonons by the composition of two E -symmetric phonons. Similarly, the magnetic excitation from the singlet ground state to the TBS mode can be interpreted as a resonance driven by the difference-frequency harmonic components of the E -symmetric phonons shown in Figs. S2d and S2e. The TBS (Fig. S2f) also has B_1 symmetry, as determined by Raman spectroscopy [S3,S4], indicating that its driving relies on the same symmetry composition ($B_1 \subset E \times E$). We comment that, because both the singlet ground state and the TBS are nonmagnetic ($S = 0$), the origin of the polarization rotation measured in $\text{SrCu}_2(\text{BO}_3)_2$ must lie in lattice (birefringence) effects, which are clearly enhanced by the spin-lattice coupling.

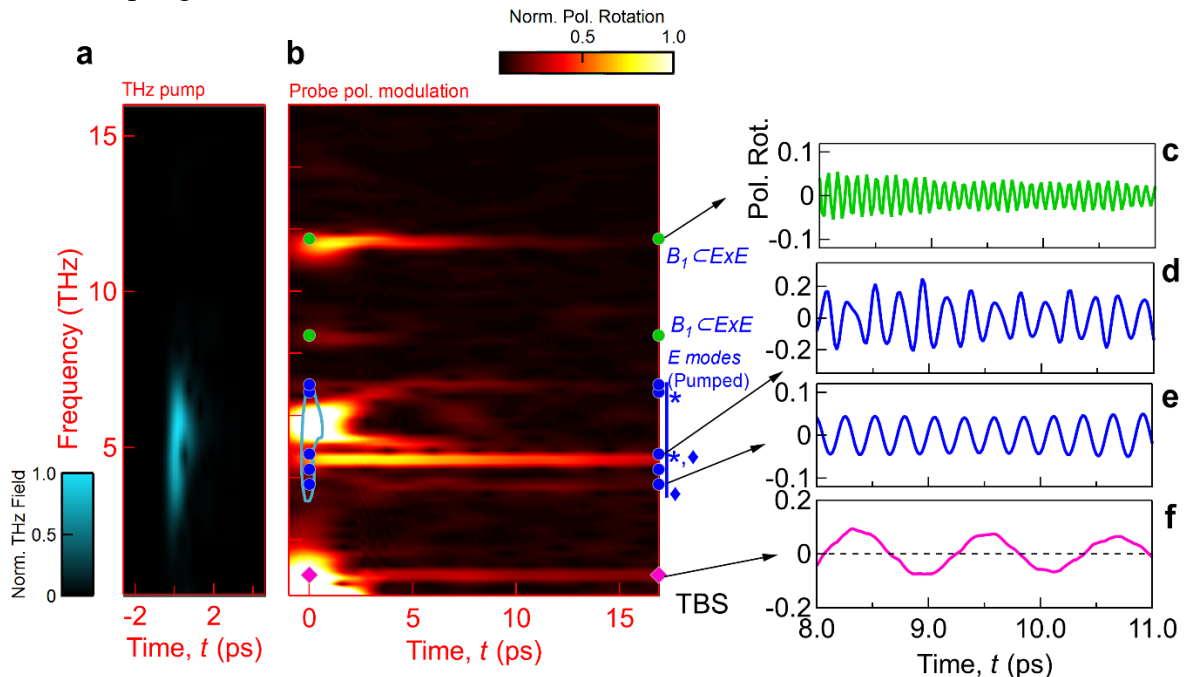


Fig. S2 | Time-frequency THz-driven dynamics. **a**, THz pump electric-field amplitude. **b**, Pump-induced polarization modulation in $\text{SrCu}_2(\text{BO}_3)_2$ at 4 K. In (a) the colour contours around $t = 0$ are based on the FWHM isoline of the amplitude. In (b) the blue circles indicate

the frequencies of the E -symmetric IR-active phonon modes that are pumped directly, which we take as 3.78, 4.27, 6.75 and 7.00 THz from Ref. [S5], whereas for the 4.60 THz mode we use our measured frequency rather than the value of 4.75 THz tabulated there. Green circles show the frequencies of B_1 -symmetric modes at 8.57 THz and 11.7 THz [S5] that are not IR-active but are excited by sum-frequency processes, which are expected to involve respectively the E -modes indicated with diamonds (3.78 THz and 4.60 THz) and with asterisks (4.60 THz and 7.00 THz). The pink diamond marks the frequency of the TBS, $\omega_{\text{TBS}} = 0.87$ THz (taken from Refs. [S3,S4]); this mode is not electromagnetically active and is driven by the nonlinear (difference-frequency) spin-phonon coupling discussed in the main text. **c-f**, Temporal dynamics, obtained by numerical band-pass filters, of the normalized polarization rotations measured for some of the primary excited modes.

Section S3. THz-driven nonlinear phonon dynamics

As summarized in the main text, the resonant dynamic distortion of the lattice in response to intense and coherent THz excitation creates nonlinear channels for the transfer of energy to both magnetic and phononic modes. The phenomenon of sum-frequency ionic Raman scattering has been investigated only recently in both experiment [S6] and theory [S7], and our results include its clearest observation to date. To describe the driven nonlinear lattice dynamics that we observe, we consider two IR-active phonons with normal coordinates q_b and q_c , with corresponding frequencies ω_b and ω_c , and a Raman-active phonon with coordinate q_R and frequency ω_R . By discarding terms quadratic in q_R , on the assumption that the amplitude of the Raman mode will be much smaller than that of the IR modes driven by the THz pump ($|q_{b,c}| \gg |q_R|$), the minimal lattice potential to cubic order (i.e. lowest anharmonic order) is

$$V(q_b, q_c, q_R) = \frac{1}{2}\omega_b^2 q_b^2 + \frac{1}{2}\omega_c^2 q_c^2 + \frac{1}{2}\omega_R^2 q_R^2 + [c_{bb,R}q_b^2 + c_{bc,R}q_b q_c + c_{cc,R}q_c^2]q_R, \quad (\text{S1})$$

where the c coefficients specify the leading nonlinear coupling terms between the IR and Raman phonons. The equation of motion for a generic THz-driven, IR-active phonon mode, m , takes the form

$$\ddot{q}_m + \gamma_m \dot{q}_m = -\frac{\partial[V - B_m q_m E_{\text{THZ}}(t)]}{\partial q_m}, \quad (\text{S2})$$

with γ_m the damping rate and B_m the dipole coupling constant introduced in Eq. (6) of the Methods section. For a phonon that is Raman-active but not IR-active, the driving term is only $\partial V/\partial q_R$. The coherent THz-driven lattice dynamics are then described in the time-domain from Eq. (S2), to leading order in q_R , by the coupled differential equations

$$\begin{cases} \ddot{q}_b + \gamma_b \dot{q}_b + \omega_b^2 q_b = -B_b E_{\text{THZ}}(t) \end{cases} \quad (\text{S3.1})$$

$$\begin{cases} \ddot{q}_c + \gamma_c \dot{q}_c + \omega_c^2 q_c = -B_c E_{\text{THZ}}(t) \end{cases} \quad (\text{S3.2})$$

$$\begin{cases} \ddot{q}_R + \gamma_R \dot{q}_R + \omega_R^2 q_R = -[c_{bb,R}q_b^2 + c_{bc,R}q_b q_c + c_{cc,R}q_c^2] \end{cases} \quad (\text{S3.3})$$

Clearly Eq. (S3.3) for the Raman phonon describes a damped harmonic oscillator driven by terms quadratic in the IR-active phonon displacements, resulting in sum-frequency excitation processes. The effectiveness of this driving will then depend on the proximity of the combinations $2\omega_b$, $2\omega_c$ and $\omega_b + \omega_c$ (and indeed $\omega_c - \omega_b$) to ω_R .

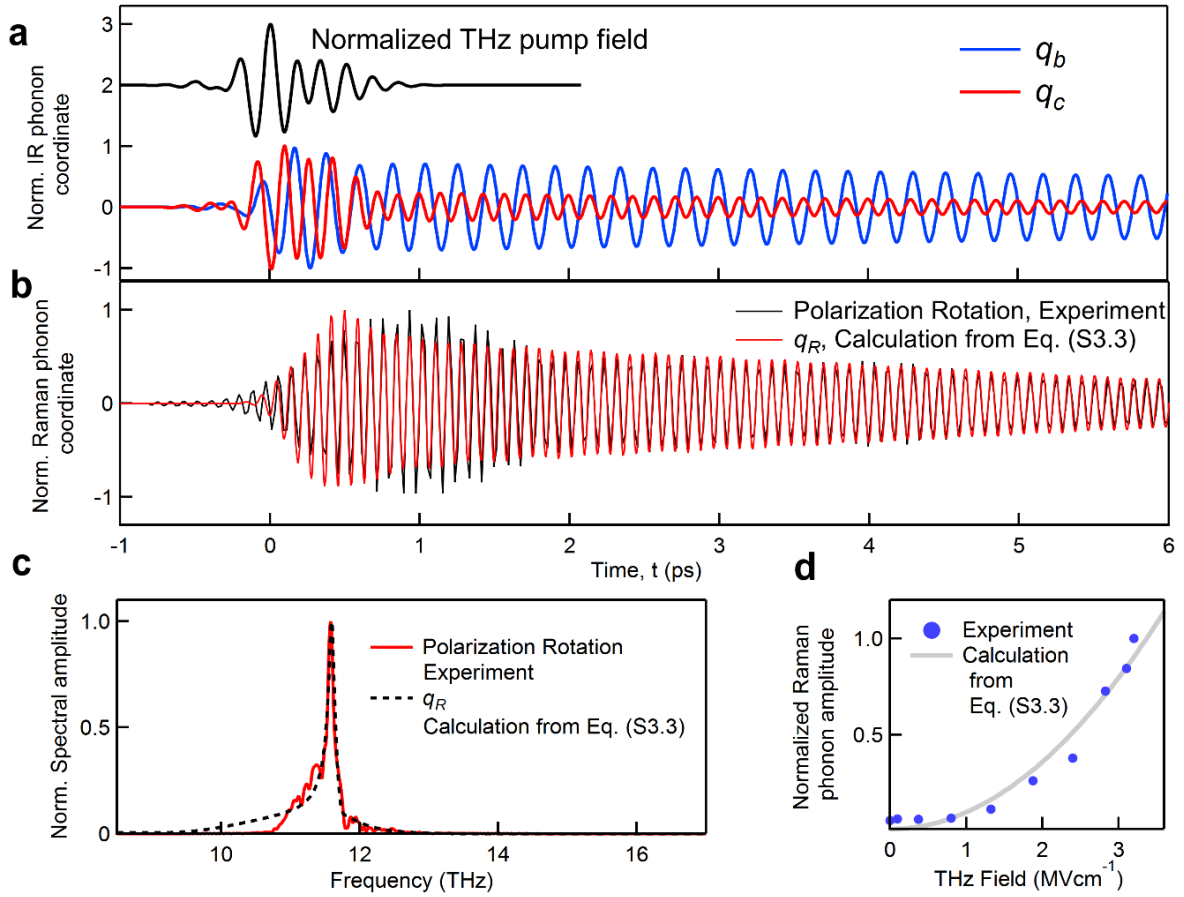


Fig. S3 | Sum-frequency ionic Raman excitation: experimental evidence and model. **a**, Normalized experimental THz driving field (black) and normalized time-dependent THz-driven atomic displacements, calculated from Eqs. (S4.1) and (S4.2), of the IR-active phonon modes q_b at $\omega_b = 4.60$ THz (blue) and q_c at $\omega_c = 7.0$ THz (red). **b**, Time-dependent phonon-driven atomic displacement, q_R , of the Raman-active phonon mode, obtained from Eq. (S3.3) and compared to the normalized polarization rotation (Fig. S2) measured by using a numerical band-pass filter to remove the components of the lower-frequency modes. **c**, Fourier-transformed amplitude of q_R and of the polarization rotation shown in panel (b). **d**, Measured amplitude of q_R compared with the quadratic electric-field dependence given by Eq. (S3.3).

The clearest example in Fig. S2b is the B_1 Raman mode with frequency $\omega_R = 11.7$ THz and damping $\gamma_R = 0.2$ THz (Fig. S2c). The two THz-pumped E -symmetric phonons marked by the asterisks have parameters $\omega_b = 4.60$ THz, $\gamma_b = 0.03$ THz and $\omega_c = 7.00$ THz, $\gamma_c = 0.10$ THz. Figure S3a shows the temporal evolution of q_b and q_c calculated from Eqs. (S3) using the experimental THz pump field. As expected from the respective phonon frequencies, the Raman coordinate, q_R , is dominated by coherent oscillations of the frequency $\omega_b + \omega_c$ (Fig. S3b), confirming the sum-frequency ionic Raman mechanism. The phenomenon is equally clear in the frequency domain, where the Fourier amplitudes of the measured and calculated dynamics are compared in Fig. S3c. Because the amplitude of q_R varies linearly with each individual amplitude q_b or q_c [Eq. (S3.3)], it should scale quadratically with the THz field strength, as Fig. S3d confirms. We stress again that all the phonon parameters used in our analysis were taken from the FTIR spectroscopy measurements of Ref. [S5], except for the phonon frequency $\omega_b = 4.60$ THz, which is the experimental value obtained by our pump-probe measurement (as

opposed to the value 4.75 THz from FTIR spectroscopy). This substitution gave a significantly better account of our measured B_1 Raman frequency of 11.58 THz. A similar analysis can be performed for the B_1 phonon mode at 8.57 THz, with driving by ω_b combined with the IR-active phonon at $\omega_a = 3.78$ THz (both marked by blue diamonds in Fig. S2b).

Section S4. Phonon modulation of magnetic interactions

We have performed a hierarchy of DFT calculations in order to obtain quantitative estimates of the effects of the driven IR phonons on the magnetic system in $\text{SrCu}_2(\text{BO}_3)_2$.

a) DFT calculations at equilibrium

First we used Quantum Espresso [S8] to perform total-energy calculations for the lattice and magnetic energies of $\text{SrCu}_2(\text{BO}_3)_2$ at equilibrium. Quantum Espresso operates in the structural unit cell of the system, which is tetragonal and contains 44 atoms (of which 8 are Cu atoms) in two ‘‘Shastry-Sutherland’’ layers. The electron-ion interactions were modelled using pseudopotentials from the curated SSSP library [S9,S10]. The plane-wave cut-off was set at 750 eV (6000 eV for the charge density) and for sampling of the Brillouin zone we used a $6 \times 6 \times 6$ k -point grid. Structural relaxation was continued until each component of the force acting at every atom was less than 0.0025 eV/\AA and the pressure (defined as $\frac{1}{3} \text{Tr}[\sigma]$, with σ being the stress tensor) was below 0.5 kbar. These parameters ensure errors smaller than 1 meV/atom within the total energy and, more importantly, smaller than 1 K on the magnetic interactions (which depend only on total-energy differences, and thus converge faster and better than do the absolute values). The lattice parameters we obtain, the $T = 0$ DFT structure, agree with the measured low-temperature structure of $\text{SrCu}_2(\text{BO}_3)_2$ [S11] to within 1% for the a and b axes and 3% for the c axis. By comparing the energies of different spin configurations computed with this structure, we fixed the value of the effective Hubbard term to $U = 11.4 \text{ eV}$ by reproducing the interaction parameters $J = 84.0 \text{ K}$ and $J' = 49.7 \text{ K}$ [S12]. The Born effective charges, Z_{eff}^i , used to estimate the maximum displacements, δ_m , in the Methods section, were computed for the system in the AFM configuration using the PHONON module of Quantum Espresso and the PBE functional [S13].

b) DFT calculations for frozen phonons

In order to extend our DFT calculations to include the nonequilibrium atomic configurations in the presence of lattice excitations, we first made a phonon symmetry analysis of the different interatomic paths. From this we deduced that the most general magnetic state in the presence of a phonon distortion q_t is characterized by ten different interaction parameters in the unit cell, two values of $J(q_t)$ and eight of $J'(q_t)$, as shown in Fig. S4. To compute this number of unknown parameters, it is necessary to work on a 2×2 supercell, meaning to use four of the basic magnetic unit cells of $\text{SrCu}_2(\text{BO}_3)_2$. In these supercell calculations we reduced the k -point grid to $2 \times 2 \times 3$, and verified that this sampling density provided essentially equivalent results.

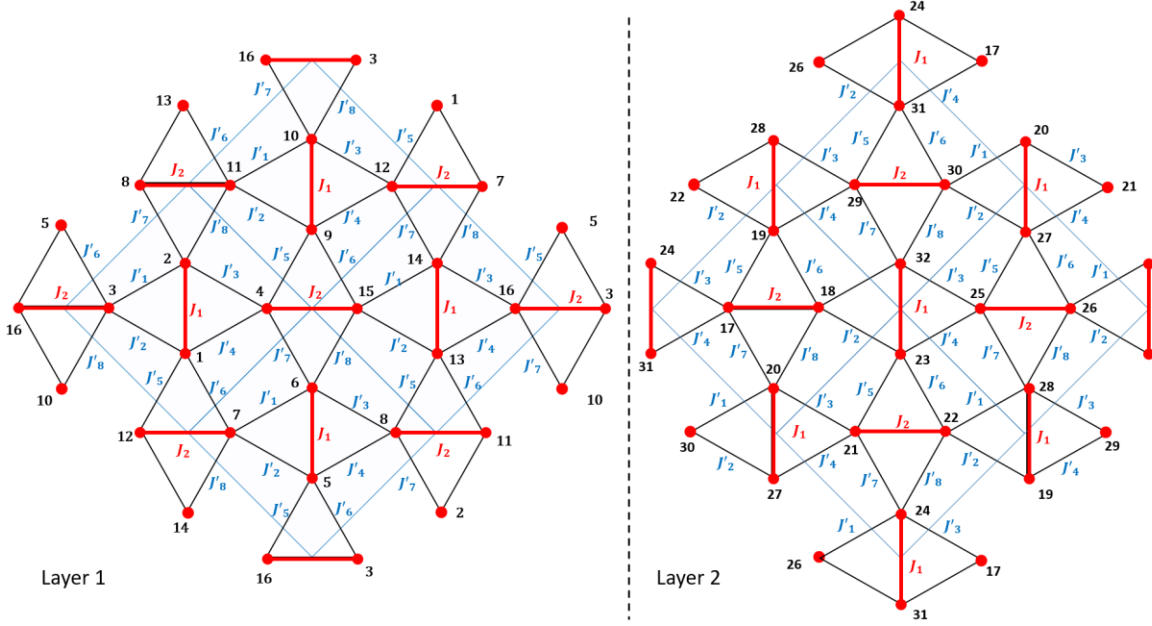


Fig. S4 | Symmetry-related magnetic interaction parameters in the spin network obtained for an arbitrary “frozen” configuration of the phonons in $\text{SrCu}_2(\text{BO}_3)_2$. Red dots represent the $S = 1/2$ spins at the Cu^{2+} sites in $\text{SrCu}_2(\text{BO}_3)_2$. For every normal mode of the lattice, the system has two different values of the intradimer interaction, J_1 and J_2 (red lines), and eight different interdimer interaction terms, J'_1, J'_2, \dots, J'_8 (black). Shown are the 2×2 supercells in each of the two layers of the structural unit cell (a total of 32 magnetic sites) required to obtain enough independent spin configurations to determine all 11 unknown parameters.

We performed total-energy calculations for the lattice structures obtained by systematic displacement of all atoms according to the normal coordinates of the strongest two phonon modes measured in experiment (Fig. 2a), q_a at $\omega_a = 3.78$ THz and q_b at $\omega_b = 4.60$ THz. While it is possible to include many more of the phonons observed in Sec. S2, here we have focused rather on optimizing our treatment of the time and frequency domains. For each distorted structure, we computed the electronic ground state as a function of the displacement amplitudes of the two phonons and for 11 different configurations of up- ($S_z = 1/2$) and down-orientated spins ($S_z = -1/2$), from which we obtained 11 linearly independent equations in order to determine all the interaction parameters in the system. This process is represented in Table S1 for one set of 11 spin configurations in Layer 1 of Fig. S4 and the corresponding equations are

$$\begin{cases}
 E(1) = E_0 + 4J_1 + 4J_2 - 6J'_1 - 2J'_2 - 6J'_3 - 6J'_4 - 6J'_5 - 6J'_6 - 6J'_7 - 2J'_8, \\
 E(2) = E_0 + 4J_1 + 4J_2 - 2J'_1 - 6J'_2 - 6J'_3 - 6J'_4 - 6J'_5 - 6J'_6 - 2J'_7 - 6J'_8, \\
 E(3) = E_0 + 6J_1 + 6J_2 - 4J'_1 - 6J'_2 - 6J'_3 - 8J'_4 - 8J'_5 - 6J'_6 - 6J'_7 - 4J'_8, \\
 E(4) = E_0 + 2J_1 + 2J_2 - 4J'_1 - 6J'_2 - 2J'_3 - 4J'_4 - 4J'_5 - 2J'_6 - 6J'_7 - 4J'_8, \\
 E(5) = E_0 + 4J_1 + 4J_2 - 6J'_1 - 6J'_2 - 6J'_3 - 2J'_4 - 6J'_5 - 2J'_6 - 6J'_7 - 6J'_8, \\
 E(6) = E_0 + 4J_1 + 4J_2 - 6J'_1 - 6J'_2 - 2J'_3 - 6J'_4 - 2J'_5 - 6J'_6 - 6J'_7 - 6J'_8, \\
 E(7) = E_0 + 6J_1 + 6J_2 - 8J'_1 - 6J'_2 - 6J'_3 - 4J'_4 - 4J'_5 - 6J'_6 - 6J'_7 - 8J'_8, \\
 E(8) = E_0 - 2J_1 - 2J_2 - 6J'_2 - 6J'_3 - 6J'_6 - 6J'_7, \\
 E(9) = E_0 - 2J'_1 - 6J'_2 - 6J'_3 + 2J'_4 - 2J'_5 - 6J'_6 - 2J'_7 - 2J'_8, \\
 E(10) = E_0 - 2J'_1 - 2J'_2 - 6J'_3 - 2J'_4 + 2J'_5 - 6J'_6 - 6J'_7 - 2J'_8, \\
 E(11) = E_0 - 2J_1 - 2J_2 + 2J'_1 - 4J'_2 - 4J'_3 - 2J'_4 - 2J'_5 - 4J'_6 - 4J'_7 - 2J'_8.
 \end{cases} \quad (\text{S4})$$

Table S1 | Eleven independent spin configurations used for one determination of the magnetic interaction parameters. Columns from 1 to 16 are the magnetic sites shown in Layer 1 of Fig. S4. 1 denotes an up-spin ($S_z = 1/2$) and -1 a down-spin ($S_z = -1/2$).

Config. #	Magnetic site															
	1	2	3	4	5	6	7	8	9	10	11	12	13	14	15	16
1	-1	-1	1	1	-1	-1	1	1	1	1	-1	-1	1	1	-1	-1
2	-1	1	-1	-1	1	1	-1	-1	-1	-1	1	1	-1	-1	1	1
3	1	1	-1	-1	1	1	-1	-1	1	-1	1	1	-1	-1	1	1
4	-1	1	-1	-1	1	-1	-1	1	1	-1	-1	1	-1	1	1	1
5	-1	-1	1	1	-1	-1	1	1	-1	-1	1	1	-1	-1	1	1
6	-1	-1	-1	1	-1	-1	1	1	-1	-1	1	1	-1	-1	1	1
7	-1	-1	1	1	-1	-1	1	1	-1	-1	1	1	-1	1	1	1
8	-1	-1	1	1	-1	-1	1	1	-1	-1	1	1	-1	-1	1	-1
9	-1	-1	1	1	-1	-1	1	1	-1	1	-1	-1	1	-1	-1	1
10	-1	-1	1	1	-1	-1	1	1	-1	1	1	-1	1	-1	-1	-1
11	-1	-1	1	1	-1	-1	1	1	1	-1	1	-1	-1	1	-1	-1

Table S2 | Magnetic interaction parameters of $\text{SrCu}_2(\text{BO}_3)_2$ calculated using the frozen-phonon protocol with all phonon displacements set to zero.

$J_1(\text{K})$	$J_2(\text{K})$	$J'_1(\text{K})$	$J'_2(\text{K})$	$J'_3(\text{K})$	$J'_4(\text{K})$	$J'_5(\text{K})$	$J'_6(\text{K})$	$J'_7(\text{K})$	$J'_8(\text{K})$
83.2	83.6	48.5	48.7	47.5	47.4	48.1	48.1	48.9	48.7

The extraction of the magnetic interaction parameters is by its nature a statistical exercise, because different spin configurations lead to different local spin densities in the DFT wavefunction, which cause subtle differences in the results for the effective J and J' parameters. We benchmark the accuracy of our statistics by testing the magnetic interactions at equilibrium (i.e. q_a and $q_b = 0$) with 100 different spin configurations and performing a least-squares regression analysis. As we show in Table S2, our results are fully consistent with the equilibrium J and J' values. The resulting statistical error on J' is 0.4 K. E_0 in Eqs. (S4) is a large constant that captures all of the nonmagnetic contributions to the calculation and cancels from the equations determining the magnetic interaction parameters.

c) DFT calculations with driven phonons

To model our experiment, in Figs. S5a-b we show the vectors, meaning the ensembles of atomic displacements, of the two primary IR-active phonons excited by the THz pump ($\omega_a = 3.78$ and $\omega_b = 4.60$ THz). We performed DFT calculations of the magnetic interactions in the presence of phonon oscillations for each phonon separately, as shown in Figs. S5c-h, and with both phonons superposed, as we show in the time series illustrated in Fig. 4d of the main text. Considering first the individual phonons, we observe that the intradimer interactions, $J_1(q_{a,b})$ and $J_2(q_{a,b})$, have a largely quadratic dependence on $q_{a,b}$ for both phonons (Figs. S5c-d), suggesting that out-of-plane O atomic motions cause the predominant effects on these parameters. By contrast, most of the interdimer interactions, $J'_i(q_{a,b})$, show strong linear as well as quadratic contributions (Figs. S5e-f) that depend both on the interaction pathway in

question and on the combination of in- and out-of-plane atomic motions. It is clear that all four difference parameters, $\Delta J_{12}(q_{a,b})$, $\Delta J_{34}(q_{a,b})$, $\Delta J_{56}(q_{a,b})$ and $\Delta J_{78}(q_{a,b})$, have strong linear contributions (Figs. S5g-h) that allow an efficient driving of two-triplon creation processes by the IR-active phonon oscillations (Methods).

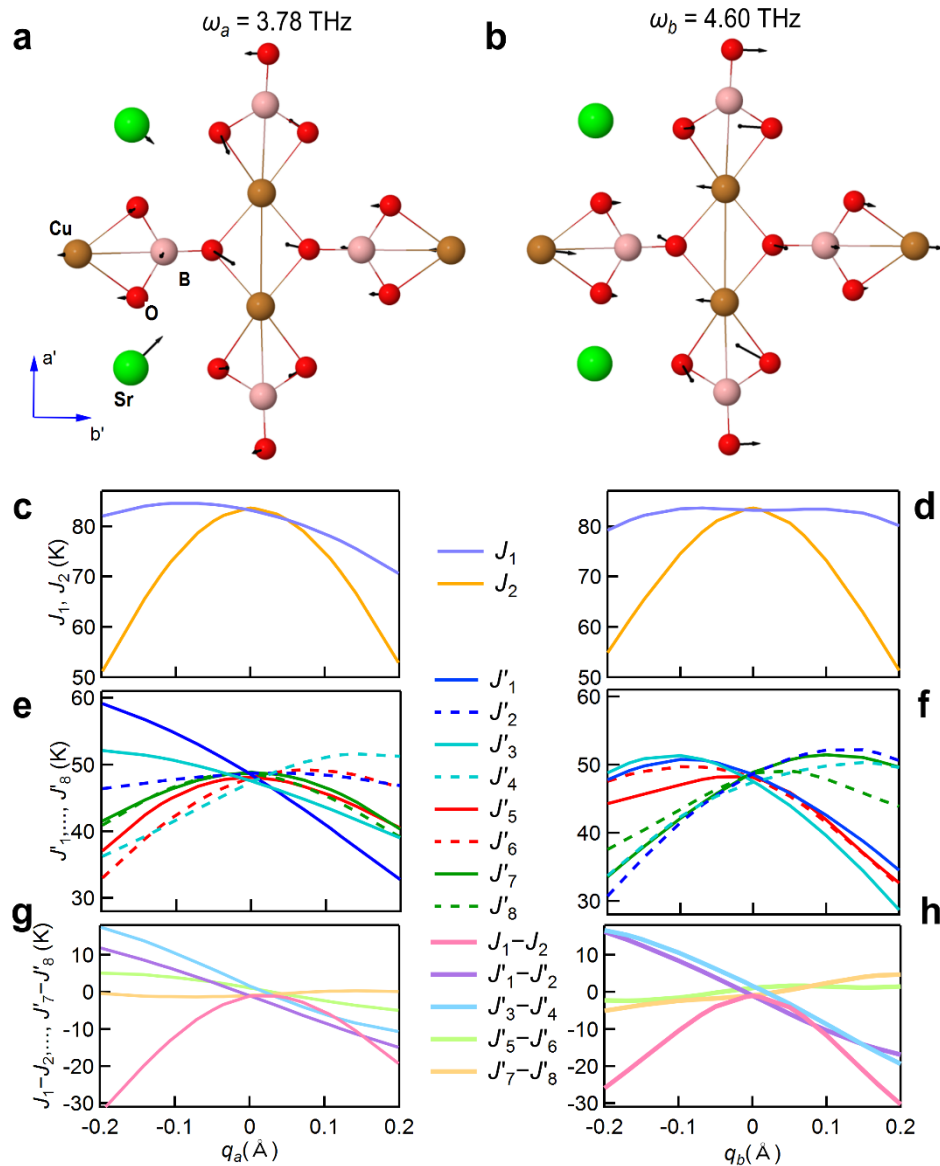


Fig. S5 | Phonon displacement vectors and calculated magnetic interaction parameters in $\text{SrCu}_2(\text{BO}_3)_2$. **a**, Atomic motions in the normal mode (q_a) of the lattice at $\omega_a = 3.78$ THz. **b**, As in panel (a) for q_b at $\omega_b = 4.60$ THz. We comment that these phonon modes are in general not symmetric between the \mathbf{a}' and \mathbf{b}' axes (Fig. 1a), but that their doublet counterparts within each E -symmetric manifold restore this symmetry. **c-d**, Intradimer interactions J_1 and J_2 shown as functions of the phonon displacement amplitudes. **e-f**, Interdimer interactions J'_1, \dots, J'_8 . **g-h**, Differences, ΔJ_{12} , ΔJ_{34} , ΔJ_{56} and ΔJ_{78} , between pairs of interdimer interaction parameters. The parameters shown in panels (c-f) were obtained using 11 spin configurations and, after verification of their systematic evolution, were centred on the results of Table S2.

For the purposes of nonlinear magnetophononics in $\text{SrCu}_2(\text{BO}_3)_2$, the strongest modulation of the $\Delta J_{i,i+1}(q_{a,b})$ interactions is produced by the 4.60 THz phonon (Fig. S5b). This is due

largely to the fact that its maximum THz-induced phonon displacement, $\delta_b = 0.17 \text{ \AA}$ (Methods), is significantly greater than that of the other phonons (at 3.78 THz we estimated the displacement $\delta_a = 0.04 \text{ \AA}$). These maximum displacements are included in the calculations shown in Fig. 4 of the main text, where we have computed the phonon-induced modulation of the magnetic interaction parameters as a time series based on the pulse durations of our experiment. For this calculation, we computed 285 points covering 10 ps with a time resolution of 0.035 ps, which accessed both the high- and low-frequency regimes to a sufficient degree that we obtained well-resolved results for all features, in particular the TBS peak.

Finally, we comment that an average over all our computed values of J and J' indicates that the averaged coupling ratio, $\alpha(q_{a,b}) = J'/J$, increases as a function of $q_{a,b}$ for both phonon modes. This leads to the results shown in Fig. 4g of the main text and to the possibility of driving the static QPT of the spin system into the plaquette phase by using the ultrafast driving of IR phonons to increase the time-averaged coupling ratio.

References

- [S1] Vicario, C., Trisorio, A., Allenspach, S., Rüegg, Ch. & Giorgianni, F. Narrow-band and tunable intense terahertz pulses for mode-selective coherent phonon excitation. *Appl. Phys. Lett.* **117**, 101101 (2020).
- [S2] Giorgianni, F., Sakai, J. & Lupi, S. Overcoming the thermal regime for the electric-field driven Mott transition in vanadium sesquioxide. *Nat. Commun.* **10**, 1159 (2019).
- [S3] Lemmens, P. *et al.* Collective Singlet Excitations and Evolution of Raman Spectral Weights in the 2D Spin Dimer Compound $\text{SrCu}_2(\text{BO}_3)_2$. *Phys. Rev. Lett.* **85**, 2605–2608 (2000).
- [S4] Gozar, A., Dennis, B. S., Kageyama, H. & Blumberg, G. Symmetry and light coupling to phononic and collective magnetic excitations in $\text{SrCu}_2(\text{BO}_3)_2$. *Phys. Rev. B* **72**, 064405 (2005).
- [S5] Homes, C. C. *et al.* Infrared spectra of the low-dimensional quantum magnet $\text{SrCu}_2(\text{BO}_3)_2$: Measurements and *ab initio* calculations. *Phys. Rev. B* **79**, 125101 (2009).
- [S6] Melnikov, A. A. *et al.* Coherent phonons in a Bi_2Se_3 film generated by an intense single-cycle THz pulse. *Phys. Rev B* **97**, 214304 (2018).
- [S7] Juraschek, D. M. & Maehrlein, S. F. Sum-frequency ionic Raman scattering. *Phys. Rev. B* **97**, 174302 (2018).
- [S8] Giannozzi, P. *et al.* Advanced capabilities for materials modelling with Quantum ESPRESSO. *J. Phys. Condens. Matter* **29**, 465901 (2017).
- [S9] Prandini, G., Marrazzo, A., Castelli, I. E., Mounet, N. & Marzari, N. Precision and efficiency in solid-state pseudopotential calculations. *npj Comput. Mater.* **4**, 72 (2018).
- [S10] Prandini, G., Marrazzo, A., Castelli, I. E., Mounet, N. & Marzari, N. A Standard Solid State Pseudopotentials (SSSP) library optimized for precision and efficiency. *Mater. Cloud Arch.* 2018.0001/v4 (2020).
- [S11] Vecchini, C. *et al.* Structural distortions in the spin-gap regime of the quantum antiferromagnet $\text{SrCu}_2(\text{BO}_3)_2$. *J. Solid State Chem.* **182**, 3275–3281 (2009).
- [S12] Radtke, G., Saúl, A., Dabkowska, H. A., Gaulin, B. D. & Botton, G. A. Electronic

structure of the quasi-two-dimensional spin-gap system $\text{SrCu}_2(\text{BO}_3)_2$: Experiment and theory. *Phys. Rev. B* **77**, 125130 (2008).

[S13] Perdew, J. P., Burke, K. & Ernzerhof, M. Generalized Gradient Approximation Made Simple. *Phys. Rev. Lett.* **77**, 3865–3868 (1996).